Supplementary material to:

Seismic velocity variations, ground deformation and the role of fluids during a low-energy seismic swarm

Eugenio Mandler[1*], Lucia Zaccarelli[1], Massimo Nespoli[2], Maria Elina Belardinelli[2], Enrico Serpelloni[1], Francesco Pintori[1], Adriano Gualandi[3], Lauro Chiaraluce[4]

[*]corresponding author

List of contents

S1: GNSS daily displacement time series

In Figure S1 we show the daily displacement time series for the GNSS sites shown in Figure 1 of the main text. Visual inspection of the GNSS time series reveals a measurable static offset only at AT04 and ATLO east components in the order of ~ 2 mm, which is roughly equal to the precision of the measures. The sub-diurnal strain precision deducible from GNSS measures, in the order of $\sim 10^{-7}$ strain (Reuveni et al., 2012), proves to be insufficient to adequately study the Umbertide 2023 seismic sequence, and therefore GNSS data will not be considered in this study.

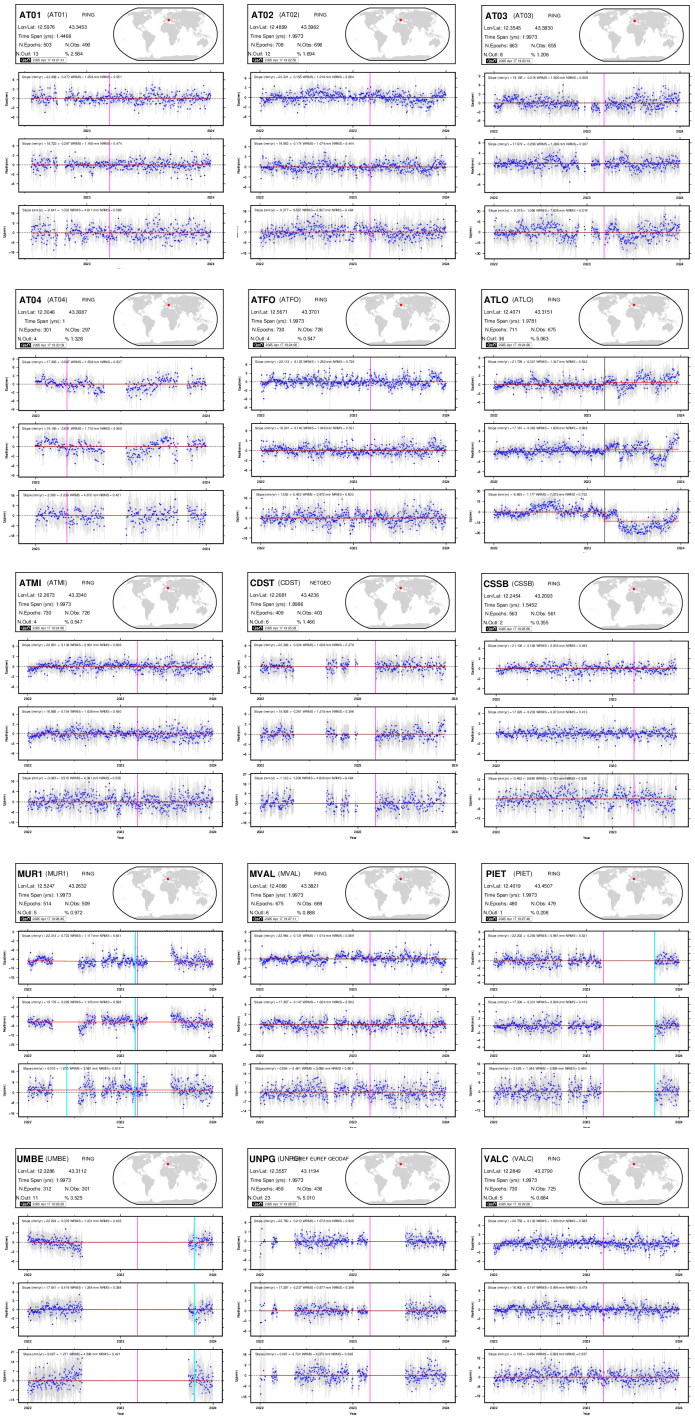
AT01 (AT01) RING
AT02 (AT02) RING
AT03 (AT03) RING
AT04 (AT04) RING
ATFO (ATFO) RING
ATLO (ATLO) RING
ATMI (ATMI) RING
CDST (CDST) NETGEO
CSSB (CSSB) RING
MUR1 (MUR1) RING
MVAL (MVAL) RING
PIET (PIET) RING
UMBE (UMBE) RING
UNPG (UNPG) RING
VALC (VALC) RING

Figure S1: GNSS daily displacement time series for the sites shown in Figure 1 of the main text. Magenta vertical lines mark the epoch of the Umbertide 2023 earthquakes whereas cyan lines indicate the epochs of antenna changes.

S2: Current cross-correlation computation

In order to retrieve crustal relative velocity variations we adopt the Moving Window Cross Spectral technique (MWCS), comparing the reference cross-correlation (CC_{ref}) to current cross-correlations (CC_{cur}) codas. As explained in Section 2.1 of the main text, CC_{ref} for each of the (east or E, north or N, vertical or Z) components of a given station pair is obtained through the stacking of the CC on the whole period analyzed. On the other hand, CC_{cur} are obtained by selecting a stacking of 25 days. We show here, as an example, the result of the tests that led to the choice of such a window length for the station pair ATVA - MURB. In practice we stack CCs over 5 to 60 consequent days, and for each stacking window length, we computed the ensamble of CC_{cur} functions applying a moving windows shifted by 1 day, and their correlation coefficient with CC_{ref}. A stacking window length = 25 days to construct CC_{cur} (vertical red lines), gives the best trade off between a good resemblance between CC_{cur} and CC_{ref} and a time resolution that allows to estimate velocity variations (Figure S2).

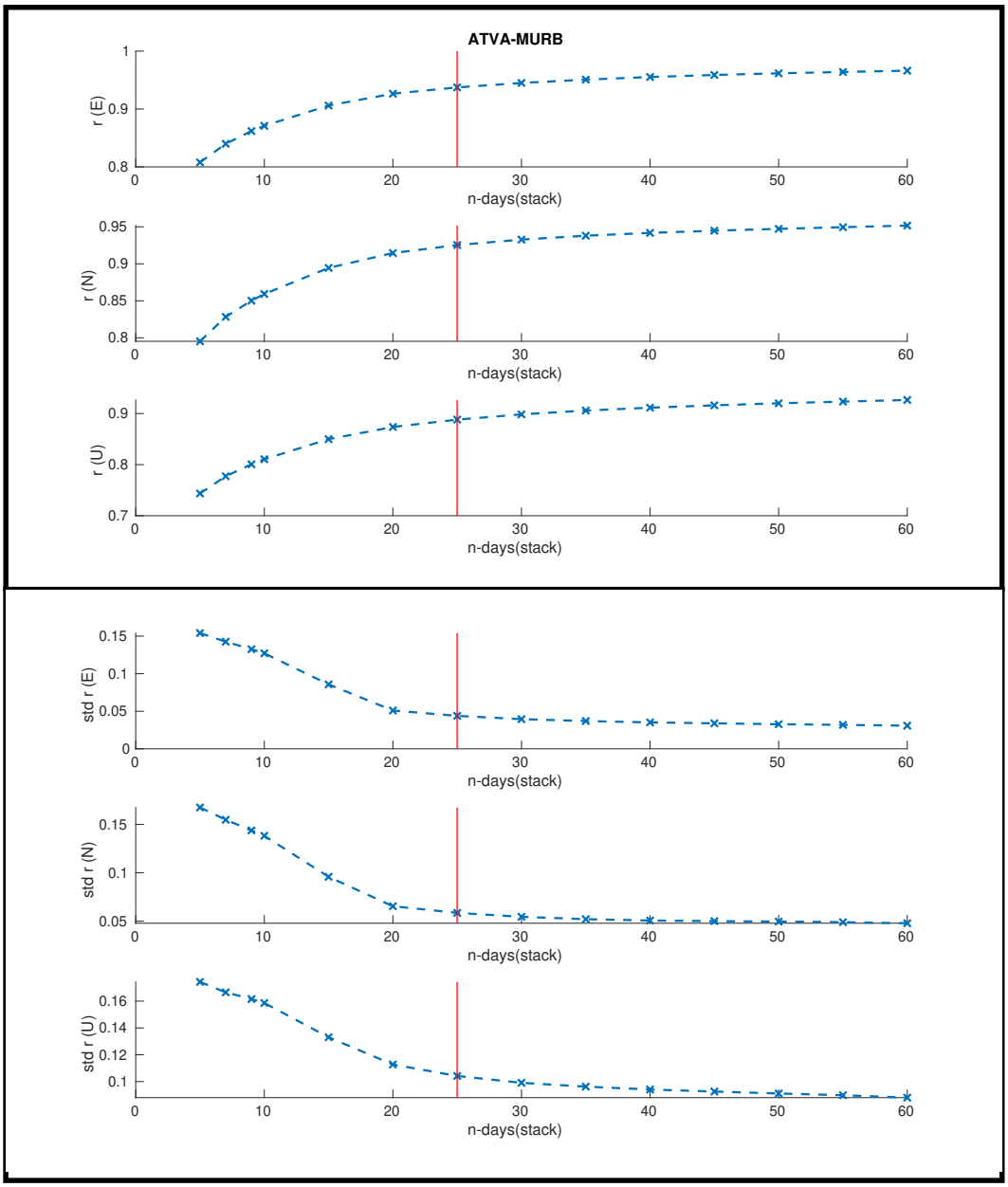
ATVA-MURB
r (E)
r (N)
r (U)
std r (E)
std r (N)
std r (U)
n-days(stack)

Figure S2: Mean and standard deviation values of the correlation coefficients r (respectively upper and lower panel) between CC_{cur} and CC_{ref} as a function of number of days used to construct the current correlation functions CC_{cur}, for the station pair ATVA-MURB.

S3: Coda assessment through RMS

As mentioned in Section 2.1 of the main text, we apply the MWCS technique to cross-correlation (CC) codas to exploit the information carried by multiple times scattered surface waves. However, the portion of CCs to be considered as coda is not univocally defined. We detail here the procedure adopted to cut CCs and to obtain the seismic waves of interest. As already mentioned in the main text, coda waves are considered to start after a time period given by the distance between the considered station pair divided by surface waves velocity of the area $\left(t_{ini} = \frac{d_{sta1-sta2}}{v_s}\right)$, $v_s = 2$ km/s. The ending arrival time of codas in the CC (t_{fin}) is selected through a root mean square (RMS) criterion, through the following steps: (1) we compute the RMS in the first 20 seconds of the CC and we call it here RSM_0; (2) we iteratively compute the RMS on CC windows 20s long, sliding them by 5s, and we call them RSM_i; (3) we fix a threshold of $2 \times RMS_0$ to distinguish coda waves from background noise. We fix the end of the coda waves when the condition $RSM_i \geq 2 \times RSM_0$ is met. This procedure is carried out for each of the three (E, N, Z) components. However, in order to be more conservative, we fix a unique time for station pair, by taking the minimum among the $(t^E_{fin}, t^N_{fin}, t^Z_{fin})$ values. An example of the results of such a procedure is given in Figure S3

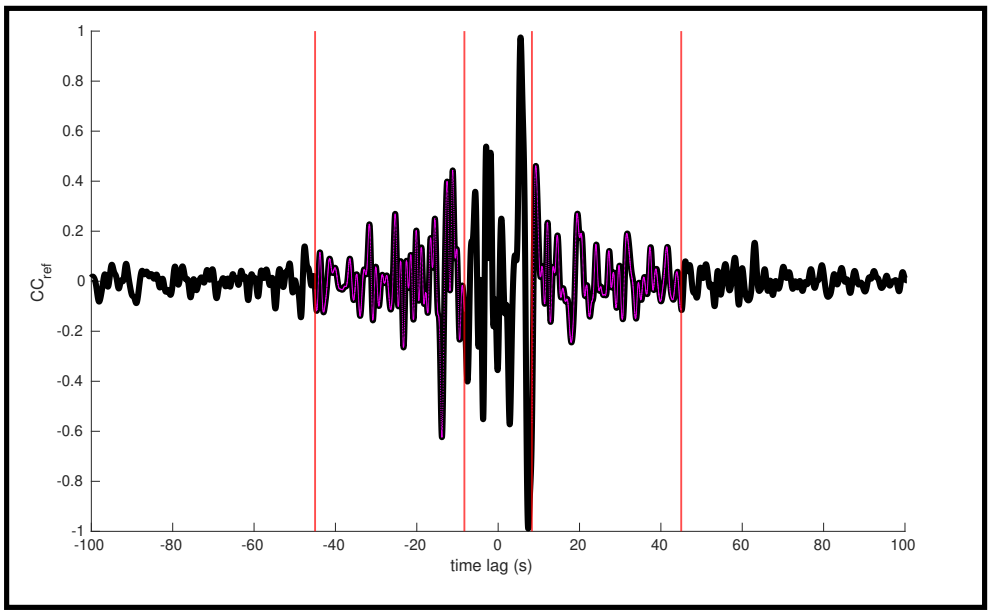
1
0.8
0.6
0.4
0.2
0
-0.2
-0.4
-0.6
-0.8
-1
CC_ref
-100
-80
-60
-40
-20
0
20
40
60
80
100
time lag (s)

Figure S3: Example of the coda waves extraction (in magenta) from the total CC_{ref} (in black), through the RMS method above-mentioned for the station pair ATFO-ATPI. Red vertical lines show the (symmetric with respect to time lag = 0) t_{ini} and t_{fin}.

S4: Strainmeter data calibration and processing

In order to get the regional horizontal strain field $\boldsymbol{\epsilon}$ from strainmeter measurements, we need to apply the calibration matrix $\boldsymbol{C}$ to the raw deformations, e_i, measured by the 4 sensors which compose a Gladwin type strainmeter (Glawdin, 1984):

$$\boldsymbol{\epsilon} = \boldsymbol{C}\boldsymbol{e} \tag{0.1}$$

or, explicitly:

$$\begin{pmatrix} AR \\ ED \\ ES \end{pmatrix} = \begin{pmatrix} C_0 & C_1 & C_2 & C_3 \\ D_{10}^{dif} & D_{11}^{dif} & D_{12}^{dif} & D_{13}^{dif} \\ D_{20}^{eng} & D_{21}^{eng} & D_{22}^{eng} & D_{23}^{eng} \end{pmatrix} \begin{pmatrix} e_0 \\ e_1 \\ e_2 \\ e_3 \end{pmatrix} \tag{0.2}$$

Calibration of the instrument belonging to the STAR array is widely covered by the paper of Hanagan et al. (2025), and in particular we follow the approach described in Supplemental Text B of that work. The calibration matrix $\boldsymbol{C}$ here employed has been derived following Mandler et al. (2024) approach and the obtained values are reported in the following table:

TSM1 (nstrain/counts)				**TSM2** (nstrain/counts)			
0.1510	0.1746	0.0338	0.1169	0.0725	0.1617	0.0807	0.0862
-0.0146	-0.0977	-0.0053	0.0030	-0.0472	-0.0087	-0.0089	-0.0417
0.1114	0.0995	-0.0213	0.0606	-0.0081	0.0442	0.0654	0.0394
TSM3 (nstrain/counts)				**TSM6** (nstrain/counts)			
-0.0117	-0.1502	-0.0919	-0.0931	-0.2583	-0.1253	-0.1865	0.0604
0.0207	0.0555	-0.0022	0.0133	-0.0151	-0.0038	0.0372	0.0063
-0.0233	-0.0484	-0.0307	-0.0442	0.0151	-0.0201	-0.0106	0.0135

Table S1: Calibration coefficients employed in this study.

An example of how 1 Hz strain data, collected at TSM1, are processed in order to remove the linear trend and the tidal related deformation is given in Figure S4, where we show the unprocessed data (black lines), the estimation of the linear + tidal components (red lines) and the residual time series (blue lines), respectively for areal strain AR (panel a), differential strain ED (panel b) and engineering strain ES (panel c). The linear + tidal components to remove are estimated through a non linear least square fitting.

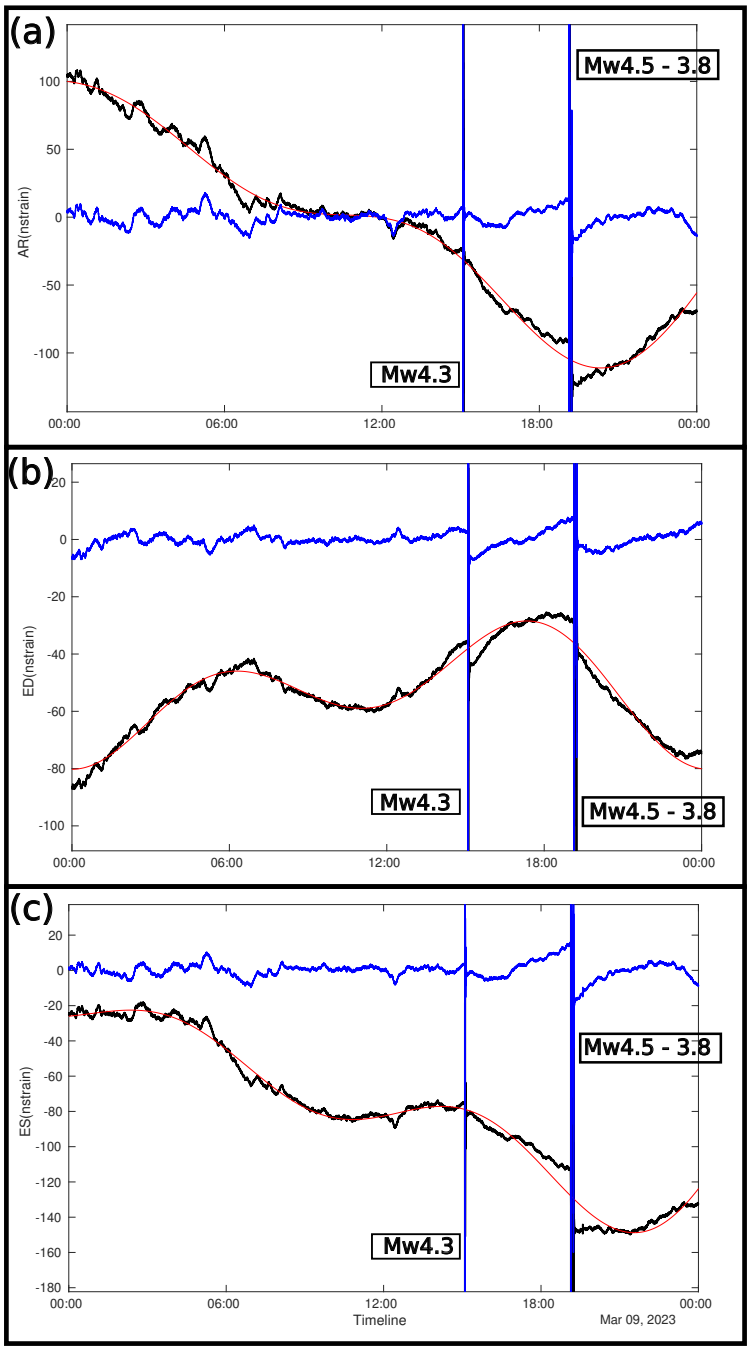
(a)
Mw4.5 - 3.8
Mw4.3
AR(nstrain)
100
50
0
-50
-100
00:00
06:00
12:00
18:00
00:00
(b)
ED(nstrain)
20
0
-20
-40
-60
-80
-100
Mw4.3
Mw4.5 - 3.8
(c)
ES(nstrain)
-120
-140
-160
-180
Timeline
Mar 09, 2023

Figure S4: Removal of the trend + tidal-related strain (red lines) from daily 1 Hz sampled time series (black lines), respectively for areal (panel a), differential (panel b) and engineering (panel c) strain components. Residuals are shown in blue.

S5: Regional temperature and rain time series

We report here the table list of the meteorological stations used to derive the temperature and rainfall time series representative of the study area (Table S2). Data are freely available from Umbria's *Servizio idrografico* web site (https://annali.regione.umbria.it/). The resulting mean daily temperature, and the detrended cumulative daily rainfall time series ($T(t)$ and $R(t)$ in the main text, Section 3.1) are shown in Figure S5 (red and blue curves, respectively).

Name	Latitude (°)	Longitude (°)
Branca	43.26028	12.68083
Carestello	43.28611	12.53417
Città di Castello	43.46139	12.25139
Compresso	43.18	12.33833
Gubbio	43.34778	12.56667
La Cima	43.23528	12.12389
Monte Cucco	43.37472	12.72917
Montedoglio	43.59150	12.05322
Montelovesco	43.30694	12.41667
Petrelle	43.34972	12.16
Pierantonio	43.26	12.38194
S. Benedetto Vecchio	43.43667	12.46389
Umbertide	43.31167	12.34722

Table S2: List of meteorological stations (thermometers and rain gauges) employed in this study to assess mean temperature and rainfall time series representative of the area.

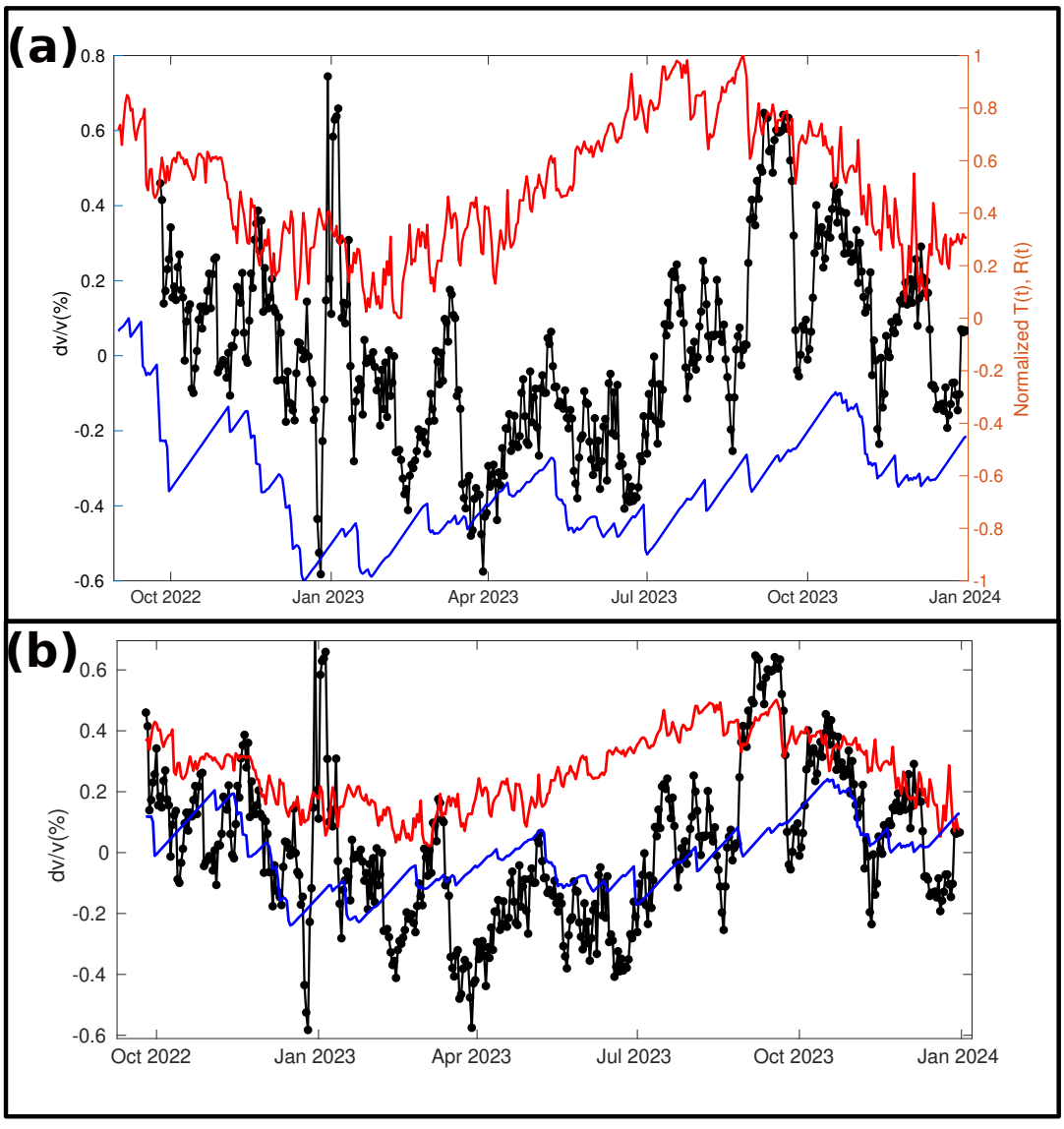
(a)
dv/v(%)
Normalized T(t), R(t)
0.8
0.6
0.4
0.2
0
-0.2
-0.4
-0.6
1
0.8
0.6
0.4
0.2
0
-0.2
-0.4
-0.6
-0.8
-1
Oct 2022
Jan 2023
Apr 2023
Jul 2023
Oct 2023
Jan 2024
(b)
dv/v(%)
0.6
0.4
0.2
0
-0.2
-0.4
-0.6
Oct 2022
Jan 2023
Apr 2023
Jul 2023
Oct 2023
Jan 2024

Figure S5 Panel (a): in black the $\frac{dv}{v}$ as in Figure 2a of the main text compared to the normalized temperature $T(t)$ (red) and rainfall $R(t)$ (blue) time series (see Section 3.1). The sign of $R(t)$ is reversed for visual comparison. Panel (b): $\frac{dv}{v}(t)$ (black curve), $\frac{dv}{v}^{T}_{syn}(t)$ (red curve) and $\frac{dv}{v}^{R}_{syn}(t)$ (blue curve) as defined in Equations 2 and 3.

S6: Peak Ground Velocity computation

We detail here the steps we followed to compute the average Peak Ground Velocity (PGV) for the study area. First we select, from the INGV bulletin (https://terremoti.ingv.it/), all the events with $M \geq 2.5$, within a $R \leq 120$ km from Umbertide. For each event in the catalog, we find the maximum velocity induced at each seismometer on the horizontal components. Since we are working mainly with Rayleigh waves, we neglect the maximum vertical velocity. For each station, we take the mean of PGV^{East} and PGV^{North} as representative of the PGV induced by each earthquake, and we average it among all sites in order to get a PGV value for the study area. Results are shown in Figure S6.

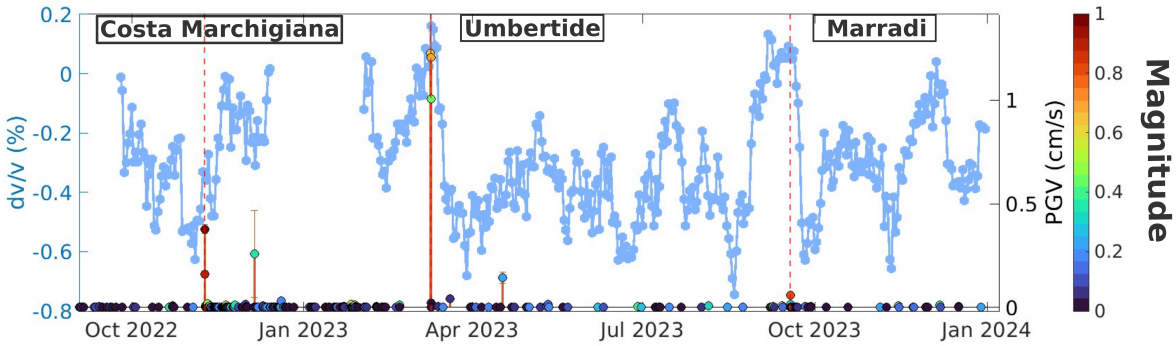

Figure S6: Peak ground velocity at the sites shown in Figure 1 (main text), for seismicity in the period September 1^{st} 2022 - December 31^{st} 2023, with $M \geq 2.5$, within a $R \leq 120$ km from Umbertide. Epochs for the earthquakes are from INGV bulletin (https://terremoti.ingv.it/). Overimposed the same dv/v of Figure 2b of the main text.

S7: dv/v frequency analysis

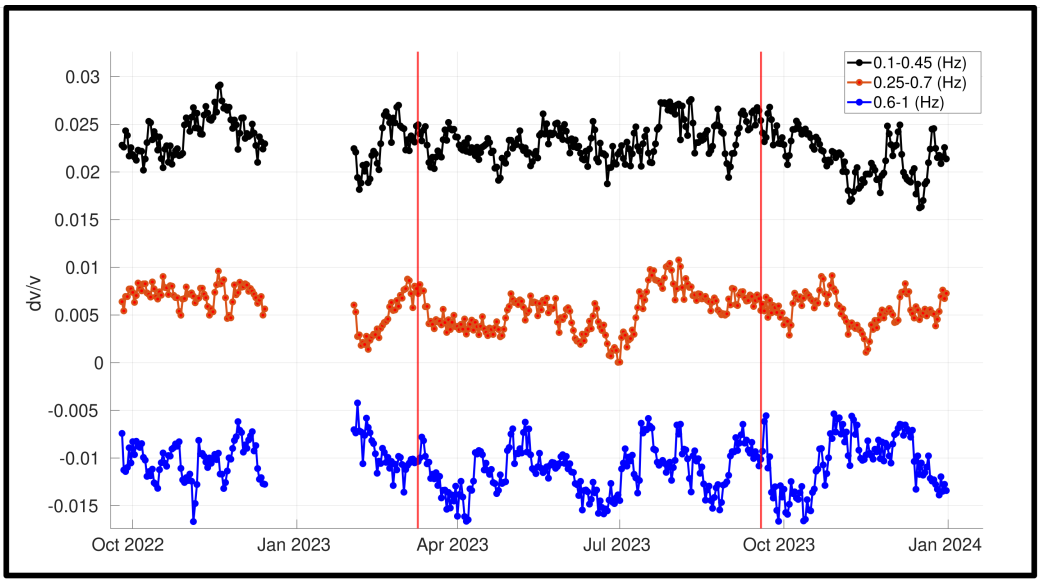

Figure S7: The $\frac{dv}{v}$ computed on different frequency bands in Hz after temperature and rainfall effects removal (see legend).

S8: High rate pore pressure data

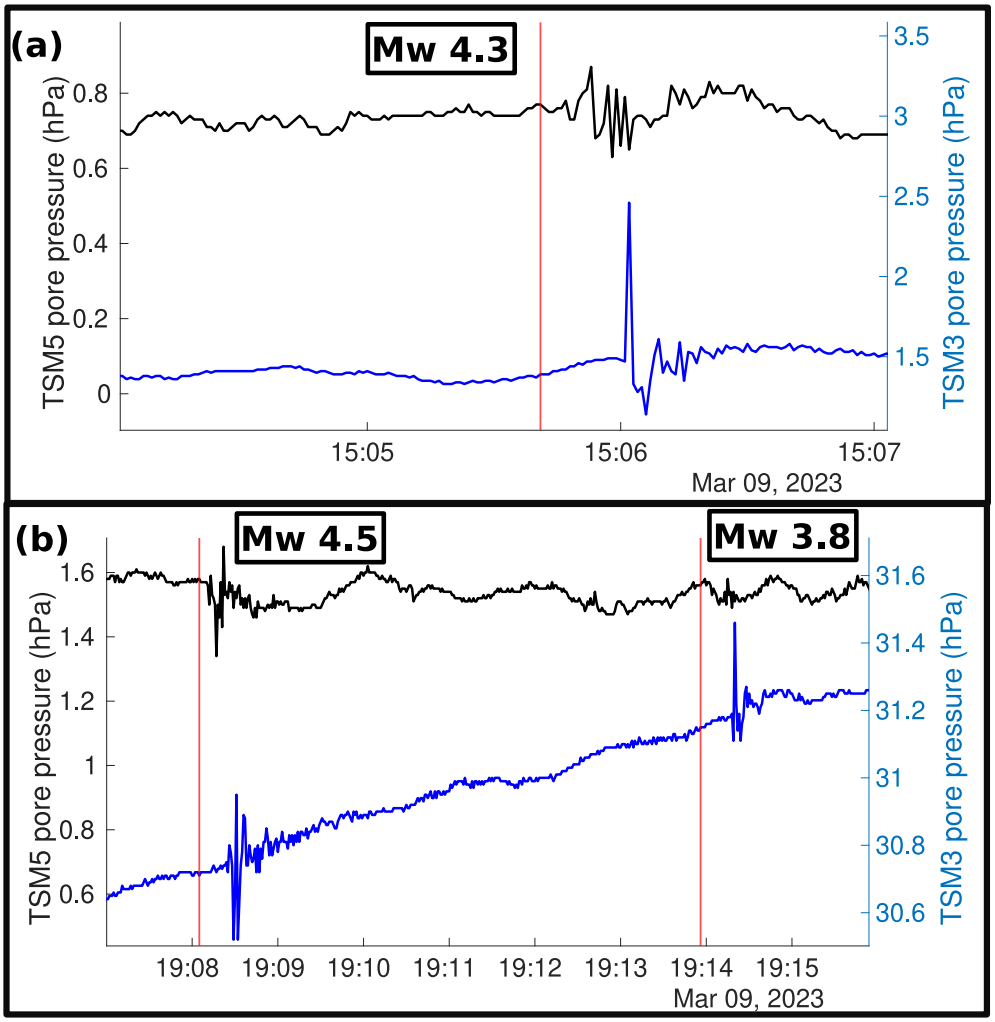

Figure S8: 1 Hz pore pressure variations at TSM3 (blue) and TSM5 (black) after the M_w 4.3 event (panel a), and after the M_w 4.5 and 3.8 events (panel b). Seismic waves' arrival time delay at TSM3 is likely related to an issue with the transducer clock.

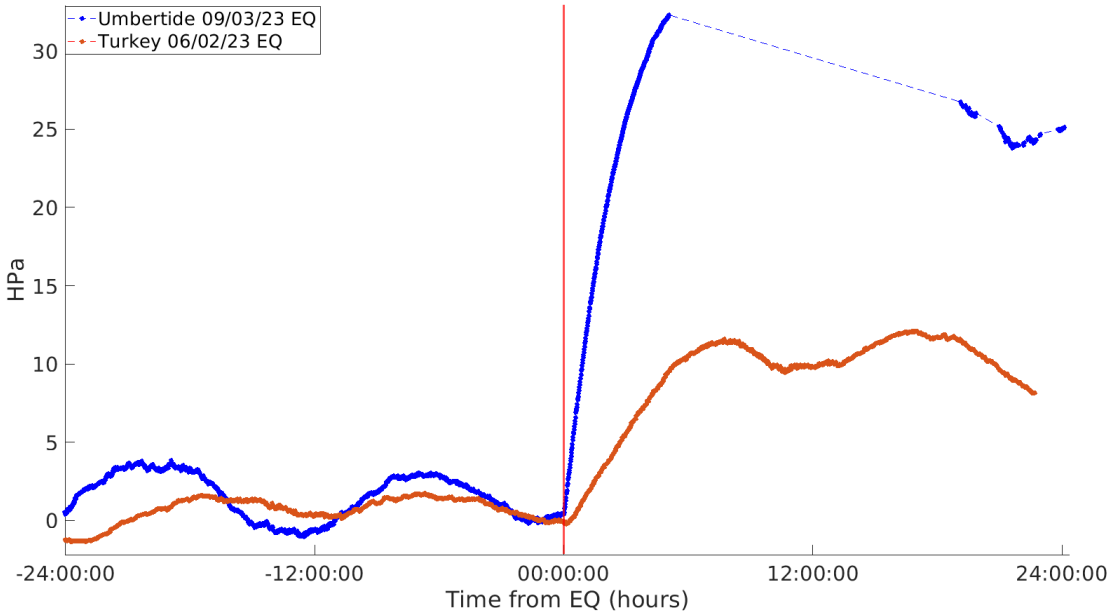

Figure S9: Pore pressure variations at TSM3 after the February 6^{th} M_w 7.8 (orange) and the M_w 4.3 Umbertide (blue) earthquakes. Time is measured from origin time of each event.

S9: Poroelastic model: additional results

The post-seismic time evolutions determined by afterslip and poroelastic rebound act, on the strainmeters, in two opposite ways. The afterslip mechanism enhances the areal contraction started during the co-seismic phase (Figure 4 of the main text), whereas the poroelastic mechanism produces an areal expansion. Here we show the results for models that combine these two opposite effects: keeping the Skempton's coefficient $B = 1$ and the effective stress coefficient $\alpha = 0.95$, we first increase the fluids-related deformation testing a hydraulic diffusivity $D = 10\ m^2/s$ (*Model 1*, Table S3). Since small earthquakes are known to have roughly the same afterslip and co-seismic moment release (Alwahedi et al., 2019), we then investigate the effects of larger post-seismic elastic slip by increasing the afterslip to coseismic moment ratio to 100%, both in the case of $D = 1\ m^2/s$ (*Model 2*) and $D = 10\ m^2/s$ (*Model 3*).

Results are reported in Figure S10: we observe that the pore pressure measured at TSM3 (panel e) is poorly explained by all of these models, both for the amplitude and time evolution.
Taking $D = 10\ m^2/s$ (*Model 1*, Figure S10) does not appear to well reproduce the post-seismic areal expansion (blue curve in panels a-d). Indeed we can fully relax the post-seismic expansion in the time span between the M_w 4.3 and 4.5, which is not what it is observed by the strainmeters. Increasing the afterslip/co-seismic moment = 100% overestimates the $\sim 1 - 1.5$ h areal contraction measured at all of the sites (*Model 2* of Figure S10). This effect can partly be smoothed taking $D = 10\ m^2/s$ (*Model 3*, Figure S10), except for TSM2 (panel b) whose post-seismic deformations are largely overestimated. Interestingly *Model 1* and *Model 3* give similar results, suggesting that, by imposing high hydraulic diffusivity, fluids-related deformation dominates over elastic relaxation. Overall, we deem an afterslip/co-seismic moment = 30% and a $D = 1\ m^2/s$ to be the best trade off between these two opposed mechanisms, and we therefore refer to it as to the *Preferred model*. Results are shown in Figure 4 of the main text.

	$D = 1\ m^2/s$	$D = 10\ m^2/s$
$\frac{Afterslip}{Coseismic \quad moment} = 30\%$	*Preferred Model (main text)*	*Model 1*
$\frac{Afterslip}{Coseismic \quad moment} = 100\%$	*Model 2*	*Model 3*

Table S3: Post-seismic models tested in this study.

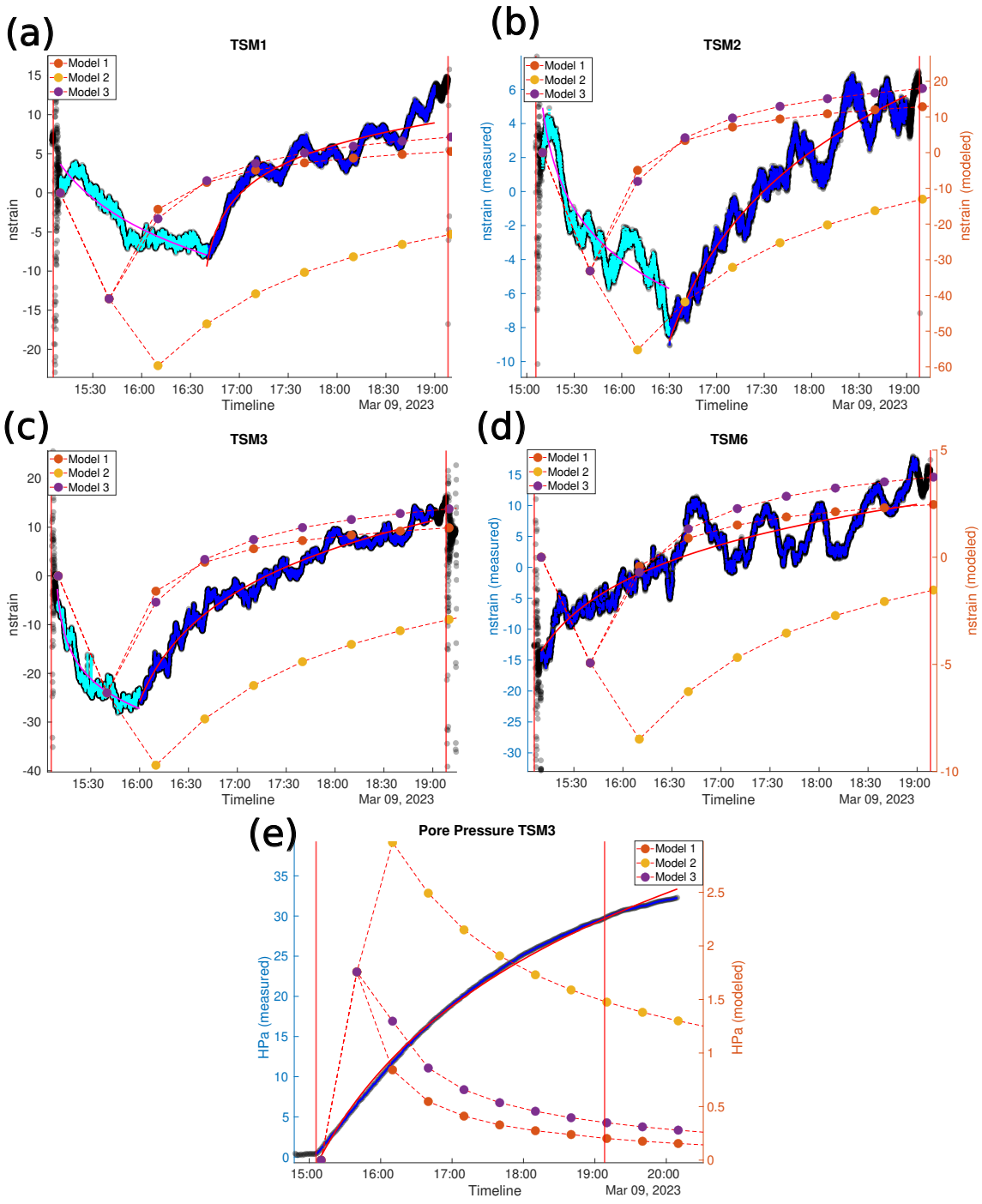
(a)
TSM1
Model 1
Model 2
Model 3
nstrain
Timeline
Mar 09, 2023
(b)
TSM2
nstrain (measured)
nstrain (modeled)
(c)
TSM3
(d)
TSM6
(e)
Pore Pressure TSM3
HPa (measured)
HPa (modeled)

Figure S10: Comparison among the post-seismic models results (see Table S3) in orange (afterslip/co-seismic moment = 30%, $D = 10\ m^2/s$), yellow (afterslip/co-seismic moment = 100%, $D = 1\ m^2/s$) and purple (afterslip/co-seismic moment = 100%, $D = 10\ m^2/s$), and the measured strain data (panel a to d) and pore pressure (panel e).

Faults interaction can be assessed through the Coulomb stress change function (*CMF*)

$$CMF = \tau - \kappa(\sigma_n - p) \tag{0.3}$$

where τ and σ_n are respectively the shear and normal stress on the receiving fault (Table S4), p is the pore pressure and κ the friction coefficient. An additional result of our poroelastic forward model is the variation of the CMF (i.e., *DCMF*), resulting from the deformation processes following the 15:05UTC M_w 4.3 earthquake, on the faults that slipped during the co- and post-seismic phase (Section 3.2 of the main text for details). We can distinguish three separated phases: the co-seismic phase (*Phase 1*, Figure S11), where the effects of the M_w 4.3 co-seismic shock are computed; the afterslip phase (*Phase 2*), when deformation is dominated by the afterslip mechanism; the poroelastic phase (*Phase 3*), when deformation is dominated by the poroelastic relaxation. We test two different κ, 0.4 and 0.7, which are the friction end members for a marnoso-arenacea formation (Collettini and Barchi, 2002). In the upper panel of Figure S11, we show the time evolution of the CMF on the fault patch where both M_w 4.3 and 4.5 nucleated. As a matter of fact, according to the INGV bullettin *https://terremoti.ingv.it/*, the two ipocenters are located only 360 m apart, and they therefore fall in the same cell of the computational grid. CMF for the $\kappa = 0.4$ and $= 0.7$ cases (respectively in purple and orange) is roughly the same during Phase 1 and 2, and they start to diverge after 17:00UTC when pore pressure variations (in blue) get more relevant. In total, during Phase 3, we observe a $\sim 10-15$ kPa re-stressing of the fault patch that slipped during the M_w 4.3 shock. The variation of the CMF (DCMF), for the whole fault plane, during the three phases is shown in the lower maps. In particular, it is evident the visible increase of stress, which favors slip on faults, on the patch where the second M_w 4.5 earthquake nucleated (gray star in map).
Despite the simplicity of the implemented forward model, and being aware of its limits, our results do not rule out the possibility that fluids readjustments after the 15:05UTC earthquake may have brought the fault patch that hosted the M_w 4.3 to slip again ~ 4 hours later with a second, larger, M_w 4.5 shock. This interpretation may suggest that, also for small earthquakes, partial ruptures are a possible explanation for the complex spatio-temporal patterns observed in nature.

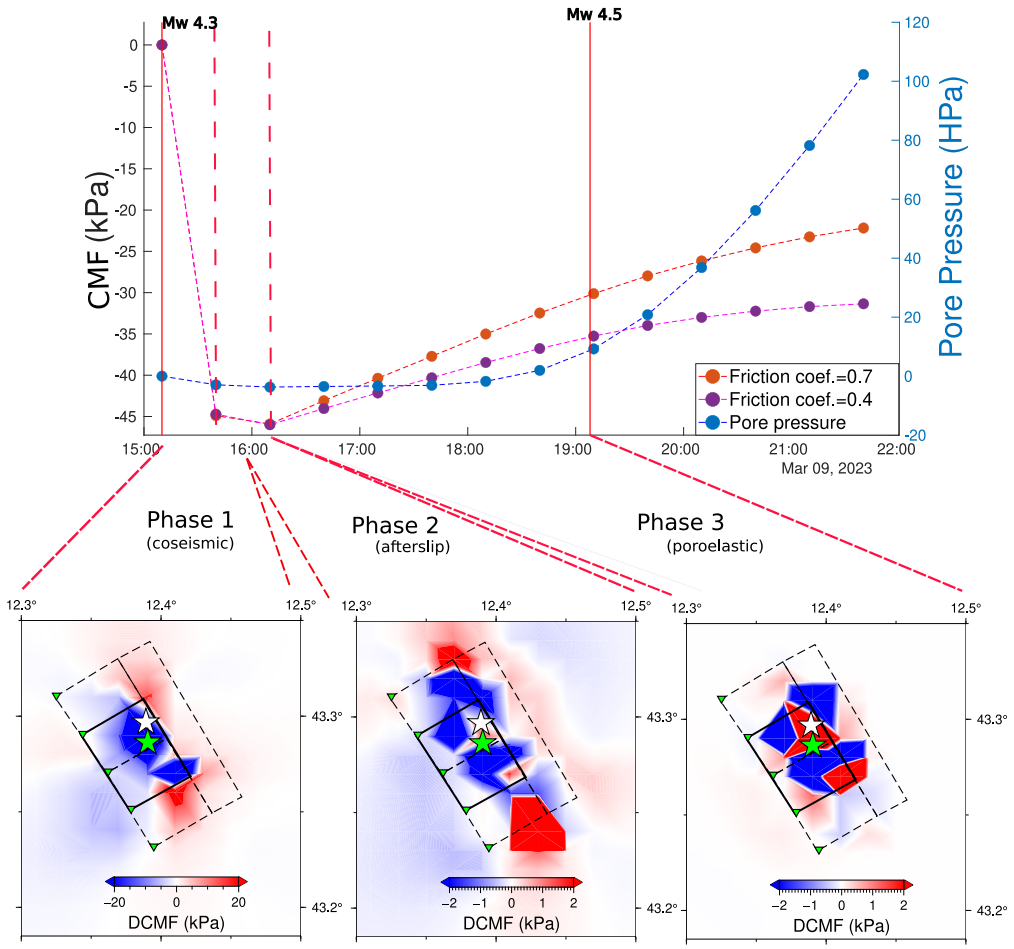

Figure S11: Upper panel: time evolution of the Coulomb stress changes (CMF) and of pore pressure on the model cell which contains both the M_w 4.3 and 4.5 hypocenters

(white and green stars, respectively). Lower panels: map of the spatial variation of the Coulomb stress (DCMF) after the coseismic phase (*Phase 1*), the phase dominated by afterslip (*Phase 2*) and the phase dominated by poroelasticity (*Phase 3*).

S10: Fault geometry parameters

Fault plane	Origin (Lat°, Lon°)	Len×Wid (km)	Strike (°)	Dip (°)	Rake (°)	Slip (m)
Coseismic	43.2508 12.3775	5×5	330	38	-50	0.0047
Afterslip 1	43.2311 12.3937	5×5	330	38	-50	5×10^{-4}
Afterslip 2	43.2703 12.3627	5×5	330	38	-50	5×10^{-4}
Afterslip 3	43.2494 12.4357	10×2.5	330	38	-50	5×10^{-4}

Table S4: Geometry of the faults used to model the coseismic and post-seismic poroelastic deformation. The origin is the top right angle of the fault plane. Slip is referred to the *Preferred Model* case (see Section S9).

S11: Marradi M_w 4.9 vs Costa Marchigiana M_w 5.5 velocity variations

In this section we discuss the short term velocity changes of Figure 2b of the main text. In order to evaluate their relevance, we make the assumption of normally distributed data and we compute the mean (μ) and standard deviation (σ). We thus take the threshold $\mu \pm 2\sigma$ to highlight significant short-term velocity variations, namely persistent positive/negative $\frac{dv}{v}$ within 25 days-long windows, which coincides with the stacking length defined in Section S2 (Figure S12). From Figure S12 we notice that only two short term $\frac{dv}{v}$ variations occur, a first (negative) one around the epoch of the Umbertide earthquakes, whereas a second (positive) one around the end of August (Figure S12). This latter is followed by a remarkable, already mentioned drop (see Section 3.1 of main text), though below the 2σ threshold, around September 20^{th} (Figure 2b, main text, and S12 Supplementary), which we think is worth discussing as it occurred only two days after the M_w 4.9 earthquake that nucleated in the northern sector of the Apennines close to the town of Marradi (*https://terremoti.ingv.it/event/36163811*). Both the August $\frac{dv}{v}$ increase and the September decrease cannot be removed by the environmental correction (Figure S5), meaning that they are only partially related to some ambient forcing or that the corrections are imperfect. Due to the limited magnitude of this earthquake and the large distance ($\sim$ 100 km) between its epicenter and the study area, following also previous authors (Bower, 1978), we neglect possible coseismic stress perturbations. In spite of that, the Marradi earthquake shook the study area with an average $PGV = 0.1$ cm/s (Figure S6) that, by using Equation 5 (main text), would give a $\epsilon_d \sim 0.5$ $\mu strain$.

In the time span analyzed, two additional moderate earthquakes (the Costa Marchigiana M_w $5.2-5.5$ shocks) occurred offshore in the Adriatic sea on the 9^{th} of November 2022, being roughly as distant as the Marradi earthquake. Estimating their relative ϵ_d, we get values $\sim 1-2$ $\mu strain$, on the other hand these events are not associated with any clear $\frac{dv}{v}$ drop (Figure S6), therefore we exclude shaking effects induced by the Marradi earthquake here. Owing to the large distance of the Marradi earthquake from the study area, we believe that the M_w 4.9 event could hardly cause such an evident velocity drop, even in the light of the comparable $\frac{dv}{v}$ surge observed around the end of August (Figure 2, main text), which is likely enhanced by the application of the thermal correction (Figure S5). Furthermore, the dv/v analysis on separate frequency bands (Figure S7) highlights a more evident drop at shallower depths (0.6-1 Hz) on September 20^{th}, whereas velocity changes at larger depths (< 0.6 Hz) are not visible for the same dates. This contrasts with the velocity changes after the Umbertide earthquakes, which are more visible at lower frequencies as already observed in this area (e.g., Zaccarelli et al., 2011; Almagro et al., 2024). This observation supports the idea of a different origin for the March and September 2023 velocity drops. The hypothesis that the drop we observe on September 20^{th} is related to some fluctuations in the $\frac{dv}{v}$ emerging from the data processing and/or correction rather than a physical variation of the mechanical properties of the crust, is also supported by the lack of a clear velocity change associated with the larger November 9^{th} M_w $5.2-5.5$ Costa Marchigiana earthquakes. Multiple seismotectonic settings are known to characterize the Italian territory (Pondrelli et al., 2020), with the Marradi earthquake belonging to the same tectonic domain as the study area (Piccinini et al., 2014), and the Costa Marchigiana earthquakes belonging to the compressional tectonic domain of the Adriatic side (e.g., Carminati et al. 2001). Even though the transmission of the earthquake related perturbation might be more favorable for the Marradi earthquake, no evidence has stood out to support this hypothesis. As we have discussed in Section 4 of the main text, the passage of seismic waves in areas rich in fluids can be significant away from the epicentral area, even in case of small pressure perturbations (Bower, 1978; Brodsky et al., 2003). However, no clear pore pressure change is measured at the TSMs sites. A more thorough investigation of the origin of this second $\frac{dv}{v}$ is beyond the scope of this study and it will possibly be addressed in future works.

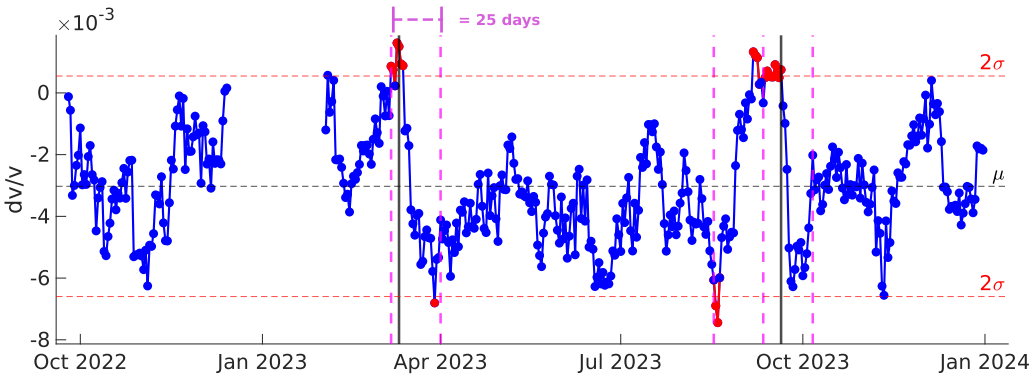

Figure S12: Same $\frac{dv}{v}$ as Figure 2b of main text, together with the mean value μ (black dashed horizontal line) and the $\mu \pm 2\sigma$ (red dashed horizontal lines) threshold. Red points mark values out of the 95.4% of $\frac{dv}{v}$ variability. Magenta dashed lines show the 25 days-long stacking time window, starting from the first point beyond the $\mu \pm 2\sigma$ threshold. Grey vertical lines mark the epochs of the Umbertide and Marradi earthquakes.

Bibliography

- Almagro Vidal, C., Zaccarelli, L., Pintori, F., & Serpelloni, E. (2024). Crustal deformation and seismic velocity perturbations in the Alto Tiberina fault zone (Northern Apennines, Italy) . Journal of Geophysical Research: Solid Earth, 129, e2024JB029023. https://doi.org/10.1029/2024JB029023

- Alwahedi, M. A., & Hawthorne, J. C. (2019). Intermediate-magnitude postseismic slip follows intermediate-magnitude (M 4 to 5) earthquakes in California. Geophysical Research Letters, , 46, 3676–3687.445 https://doi.org/10.1029/2018GL081001

- Bower, D. R., and K. C. Heaton (1978) Response of an aquifer near Ottawa to tidal forcing and the Alaskan earthquake of 1964, Can. J. Earth Sci., , 15, 331 – 340, 1978.

- Brodsky E., Roeloffs E., Woodcock D., Gall I., and Manga M. (2003). A mechanism for sustained groundwater pressure changes induced by distant earthquakes, J. Geophys. Res. , 108(B8), 2390, doi:10.1029/2002JB002321.

- Carminati, E., Toniolo Augier, F., & Barba, S. (2001). Dynamic modelling of stress accumulation in Central Italy: Role of structural heterogeneities and rheology. Geophysical Journal International, 144, 373390.https://doi.org/10.1046/j.1365-246x.2001.00323.x

- Collettini, C., and Barchi, M. R. (2002). A Low-Angle normal Fault in the Umbria Region (Central Italy): A Mechanical Model for the Related Microseismicity. Tectonophysics, 359, 97–115, doi:10.1016/S0040-1951(02)00441-9

- Hanagan, C., Mandler, E., Bennett, R., Chiaraluce, L., Gottlieb, M., Gualandi, A., Hughes, A., Johnson, W., Mencin, D., & Marzorati, S. (2025). Characterization and validation of tidally calibrated strains from the Alto Tiberina Near Fault Observatory Strainmeter Array (TABOO-NFO-STAR). Seismica, 4(1). https://doi.org/10.26443/seismica.v4i1.1471

- Gladwin, M. T. (1984). High precision multi component borehole deformation monitoring. Review of Scientific Instruments, 55, 2011–2016.

- Mandler, E., Canitano, A., Belardinelli, M.E., Nespoli, M., Serpelloni, E., Linde, A. (2024). Tidal Calibration of the Gladwin Tensor Strain Monitor (GTSM) Array in Taiwan. Pure Appl. Geophys., https://doi.org/10.1007/s00024-024-03453-9

- Pondrelli, S., Visini, F., Rovida, A., D'Amico, V., Pace, B., & Meletti, C. (2020). Style of faulting of expected earthquakes in Italy as an input for seismic hazard modeling. Natural Hazards and Earth System Sciences , 20,3577. doi:10.5194/nhess-20-3577-2020

- Reuveni, Y., Kedar, S., Owen, S. E., Moore, A. W., and Webb, F. H., (2012). Improving sub-daily strain estimates using GPS measurements. *geophys. Res. Lett., 39, L11311, doi:10.1029/2012GL051927.*

- Zaccarelli, L., Shapiro, N.M., Faenza, L., Soldati, G. & Michelini, A. (2011). Variations of crustal elastic properties during the 2009 L'Aquila earthquake inferred from cross correlations of ambient seismic noise. geophys. Res. Lett., 38(L24304). doi:10.1029/2011GL049750.